ACS OMEGA

http://pubs.acs.org/journal/acsodf

Article

Novel Adamantane-Linked Isothiourea Derivatives as Potential Chemotherapeutic Agents: Synthesis, Structural Insights, and Antimicrobial/Anti-Proliferative Profiles

Fatmah A. M. Al-Omary, Natalia Alvarez,* Lamees S. Al-Rasheed, Nicolás Veiga, Hanan M. Hassan, and Ali A. El-Emam*

Cite This: *ACS Omega* 2023, 8, 13465−13477

Read Online

ACCESS | Metrics & More | Article Recommendations | Supporting Information

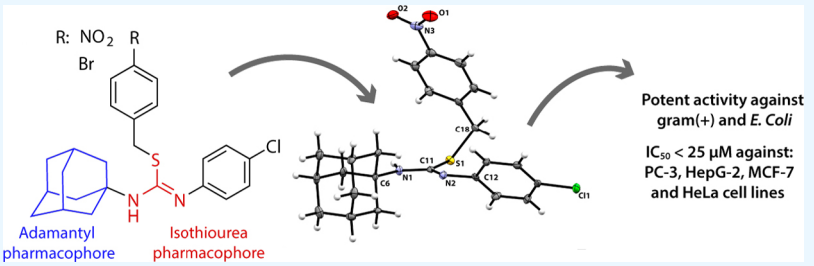

ABSTRACT: In this study, two adamantane-linked isothiourea derivatives containing a common 4-chlorophenyl substituent coupled with 4-nitrobenzyl or 4-bromobenzyl moieties were synthesized. Both derivatives were characterized, in the solid state and in solution, through a synergistic combination of experimental and in silico techniques, and the results are of great value for the chemical and structural characterization of related compounds. The crystal structures of both derivatives were analyzed in depth, including Hirshfeld surface analysis and lattice energy calculations, revealing a predominant dispersive component of the total energy that stabilizes crystal packing. Both compounds showed potent broad-spectrum antibacterial activity and moderate activity against the pathogenic fungus *Candida albicans*. In addition, in vitro anti-proliferative activity assays showed that the 4-bromobenzyl analogue displays higher activity than the 4-nitrobenzyl one, with IC_{50} values under 30 μM against five human cancer cell lines. Our results give evidence of the potential of the adamantane/isothiourea combination to render auspicious scaffolds for new potential chemotherapeutic agents.

1. INTRODUCTION

As a result of the evolution of new resistant bacterial, fungal, and viral strains, the development of new chemotherapeutic agents is becoming the major interest in many academic and industrial research laboratories with the aim to discover novel, more potent molecules, with higher specificity and reduced toxicity than the existing drugs. Adamantane nucleus was early recognized as an essential building block in various chemotherapeutic agents.[1−3] The chemotherapeutic efficacy of adamantane-based drugs was early explored after the discovery of amantadine[4,5] and rimantadine[6] as potent therapy against Influenza A viral infection. Tromantadine,[7] an adamantane-based analogue, was further developed as a potent drug for the treatment of skin infection caused by herpes simplex virus (HSV). The adamantane−ethylenediamine derivative SQ109 and the related dipiperidine derivative SQ609 were recently approved as efficient therapies against drug-susceptible and drug-resistant *Mycobacterium tuberculosis* strains.[8,9] The adamantane-based anticancer agents Adaphostin,[10] Adarotene,[11] CD437,[12] and Opaganib[13] are currently utilized for the treatment of advanced cancers (Figure 1).

On the other hand, thiourea and isothiourea derivatives were reported to exhibit diverse chemotherapeutic activities including anticancer,[14−16] anti-HIV,[17,18] anti-tuberculosis,[19] and antimalarial activities.[20]

In view of the previously reported observations and as a continuation of an interest in chemotherapeutic properties,[21−24] and structural informatics[25−29] of adamantane-based derivatives, we report herein the synthesis, characterization, solid-state structural features, electronic properties, vibrational spectroscopy, and preliminary antimicrobial and antiproliferative activities of two adamantane-linked isothiourea derivatives.

Received: March 4, 2023
Accepted: March 20, 2023
Published: March 30, 2023

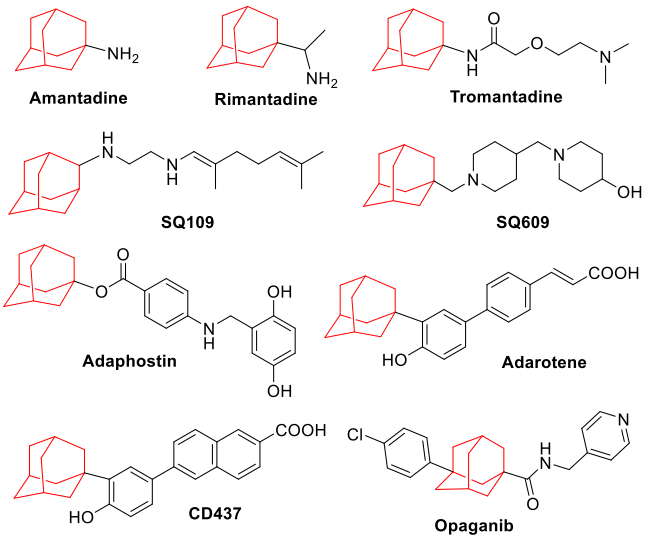

Figure 1. Structures of currently used adamantane-based chemotherapeutic agents.

2. RESULTS AND DISCUSSION

2.1. Synthesis and Crystallization. The synthesis of compounds **1** and **2** started with the reaction of adamantane-1-amine **A** with 4-chlorophenyl isothiocyanate **B** via heating in ethanol to yield 1-(adamantan-1-yl)-3-(4-chlorophenyl)-thiourea **C**.[30] Although the thiourea derivative **C** exists as a thione tautomer in the solid state,[30] the possibility of existence of the thiol tautomers **D** and **E** in the solution state is not excluded. The reaction of the thiourea derivative **C** with 4-nitrobenzyl bromide or 4-bromobenzyl bromide, in acetone, in the presence of anhydrous potassium carbonate yielded the isothiourea derivatives **1** and **2**, respectively, rather than the isomeric isothioureas **3** and **4** (Scheme 1) The structure elucidation of compounds **1** and **2** were based by ^{1}H NMR, ^{13}C NMR, elemental analysis, and electrospray ionization mass spectroscopy (ESI/MS). The ^{1}H NMR spectra of compounds **1** and **2** in $CDCl_3$ showed the adamantane protons (15H) as three distinguished peaks, a multiplet at δ 1.52−1.68 (6H) and two singlets at δ 1.98 (6H) and 2.05−2.12 (3H) ppm. Benzylic CH_2 was shown as singlets at δ 4.26 and 4.23 ppm for compounds **1** and **2**, respectively. The aromatic and NH protons (5H) were properly shown in the ^{1}H NMR spectra. The ^{13}C NMR spectra showed the adamantane carbons as four characteristic peaks at δ 29.51 and 28.90, 36.25 and 35.95, 41.79 and 41.12, and 53.65 and 52.88 ppm for compounds **1** and **2**, respectively. The benzylic CH_2 carbons were shown at δ 35.95 and 36.44 ppm, and the C═N carbons were shown at δ 153.66 and 151.98 ppm. In addition, the aromatic carbons were shown as 8 peaks in the expected regions. The ESI/MS spectra clearly showed their positive molecular ion peak $[M + H]^+$ as the major peak. In addition, the single crystal X-ray analysis excluded the possibility of formation of the isomeric derivatives **3** and **4** and confirmed the configuration of the compounds which exist as the *Z* conformers.

2.2. Solid-State Structural Features. Crystal structures corresponding to compounds **1** and **2** were determined; both compounds crystallize in the monoclinic $P2_1/c$ space group. A summary of the crystallographic data and structure refinement parameters are listed in Table 1. Ortep representation at 50% probability for the asymmetric units of **1** and **2** is depicted in Figure 2.

In the case of compound **2**, the asymmetric unit contains two structurally independent molecules; however, overlay similarity between molecules A and B is 0.999. For molecule description and intramolecular bond analysis, they will be treated as equivalent and molecule A will be used as the

Scheme 1. Synthetic Approach for Compounds 1 and 2

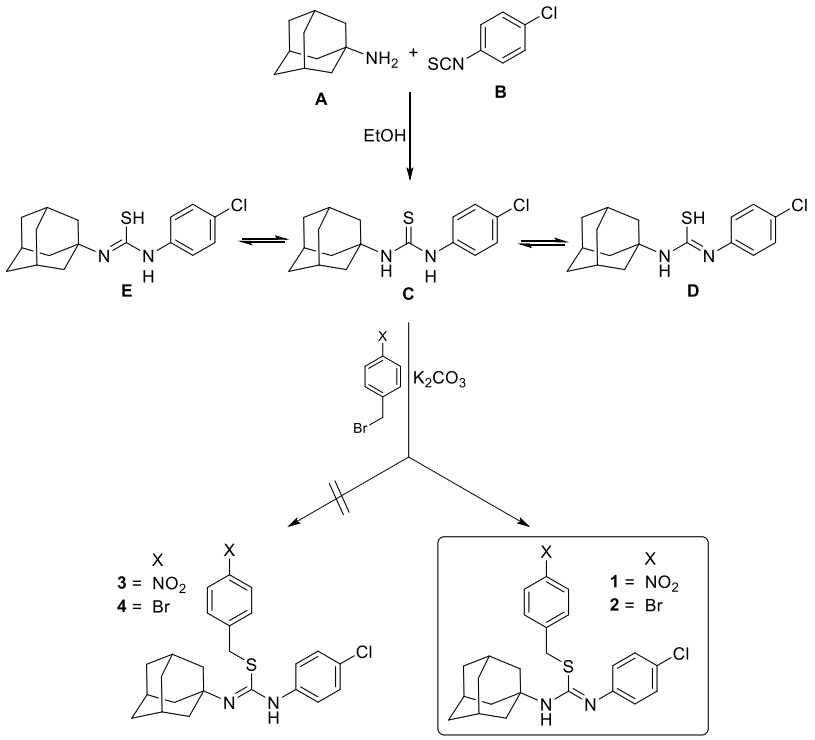

https://doi.org/10.1021/acsomega.3c01469
ACS Omega 2023, 8, 13465−13477

Table 1. Summary of Crystal Data and Structure Refinement Parameters for Compounds 1 and 2

identification code	compound 1	compound 2
empirical formula	$C_{24}H_{26}ClN_3O_2S$	$C_{24}H_{26}BrClN_2S$
formula weight	455.99	489.89
temperature	296(2) K	100(2) K
crystal system	monoclinic	monoclinic
space group	$P2_1/c$	$P2_1/c$
unit cell dimensions	a = 6.9133(4) Å	a = 12.3124(6) Å
	b = 23.4857(15) Å	b = 24.4115(12) Å
	c = 13.6428(9) Å	c = 14.7777(8) Å
	β = 98.409(2)°	β = 90.528(2)°
volume	2191.3(2) Å^3	4441.5(4) Å^3
Z	4	8
density (calculated)	1.382 Mg/m^3	1.465 Mg/m^3
absorption coefficient	0.297 mm^{-1}	2.079 mm^{-1}
F(000)	960	2016
crystal size	0.59 × 0.36 × 0.20 mm^3	0.37 × 0.37 × 0.13 mm^3
theta range for data collection	2.30−25.00°	2.16−25.00°
index ranges	$-8 \le h \le 8$, $-27 \le k \le 27$, $-3 \le l \le 16$	$-12 \le h \le 14$, $-29 \le k \le 29$, $-17 \le l \le 17$
reflections collected	3854	46,372
independent reflections	3854 [R(int) = 0.0000]	7812 [R(int) = 0.0933]
completeness (theta 25°)	99.9%	99.9%
max. and min. transmission	0.9436 and 0.8441	0.7811 and 0.5150
data/restraints/parameters	3854/0/288	7812/0/531
goodness-of-fit on F^2	1.163	1.015
final R indices [$I > 2\sigma(I)$]	R_1 = 0.0682, wR_2 = 0.1695	R_1 = 0.0397, wR_2 = 0.0887
R indices (all data)	R_1 = 0.0775, wR_2 = 0.1737	R_1 = 0.0584, wR_2 = 0.0976
largest diff. peak and hole	0.573 and −0.601 e Å^{-3}	0.602 and −0.509 e Å^{-3}
CCDC number	1906754	2211104

reference. This is not the case of intermolecular interaction analysis in which they will be studied independently. Selected bond lengths and angles in the carbamimidothioate group are shown in Table 2.

In favor of confirming the multiplicity of the N2−C11 and N1−C11 bonds, a detailed statistical analysis was performed on Mogul using the CSD database, version 5.42, including the February 2021 update.[31] Details are included in Figures S1−S4. Data support a double-bond character for N2−C11, whereas a simple bond character is evidenced for the N1−C11 bond, in agreement with similar structures previously reported.[32,33] Together with the residual density found near the N1 atom, it confirms that N1 is protonated in both structures.

To furnish a picture of the intramolecular interactions that support the specific conformation that 1 and 2 adopt in space (Figure 2), we optimized both molecules in the gas phase by DFT and carried out a topological analysis of the noncovalent interactions.[34] The results, depicted in Figure 3, reveal a series of intramolecular CH···N and CH···π interactions at play, which stabilize the particular molecular conformation found crystallographically (see the crystal structures superimposed in yellow). In general terms, the adamantyl moiety establishes two CH···N H-bonds with the isothiourea group, with binding energies ranging from 1.48 to 1.80 kcal/mol.[35] The molecular spatial configuration is also determined by the establishment of CH···π interactions between the 4-nitrobenzyl and 4-chlorobenzyl or 4-bromobenzyl and adamantyl groups for 1 and 2, respectively.

Intermolecular interactions in the crystal structures were analyzed through Hirshfeld surface analysis. To that end, a d_{norm} mapped Hirshfeld surface was generated on Crystal explorer to assess the potential hotspots for bonding interactions. Figure 4a depicts the d_{norm} surface for compound 1 with superposition of selected adjacent molecules near bonding hotspots. Atoms involved in contacts around the hotspots are indicated with colored arrows. Figure 4b,c presents the 2D fingerprint plot and percentage contact contributions to the surface by the atom type, respectively. A particular feature that stands out from the 2D fingerprint plot is the lack of the characteristic sharp spikes corresponding to the presence of an intermolecular H-bonding network. In this case, the shape of the plot, the high H···H contact contribution to the surface (53.1%), together with the H···H distances being the shortest d_e vs d_i points, suggest an intermolecular bonding scheme with a major dispersion contribution. Lattice energy calculations were performed in order to understand the nature of the intermolecular interactions' energies.

In the case of compound 2, the symmetrically inequivalent molecules A and B were treated independently. Even though the molecules are not crystallographically equivalent, in general terms, the same contact distribution is observed for both A and B. H···H contact contribution is the most significant (51.5 and 54.7% for A and B, respectively) and H···H distances being the shortest d_e vs d_i points suggests that, as observed for 1, the dispersion energy is the most energetic factor within lattice energy. Nonclassical H-bonding can be observed through Br···H, Cl···H, and S···H contacts that account for 21−25% of the total percentage contribution to the surface (Figure 5). However, when lattice energy is analyzed, the electrostatic component for the total energy of each studied pair is not the main factor.

Tables S1 and S2 present a full list of lattice energy calculations for paired molecules in compounds 1 and 2

https://doi.org/10.1021/acsomega.3c01469
ACS Omega 2023, 8, 13465−13477

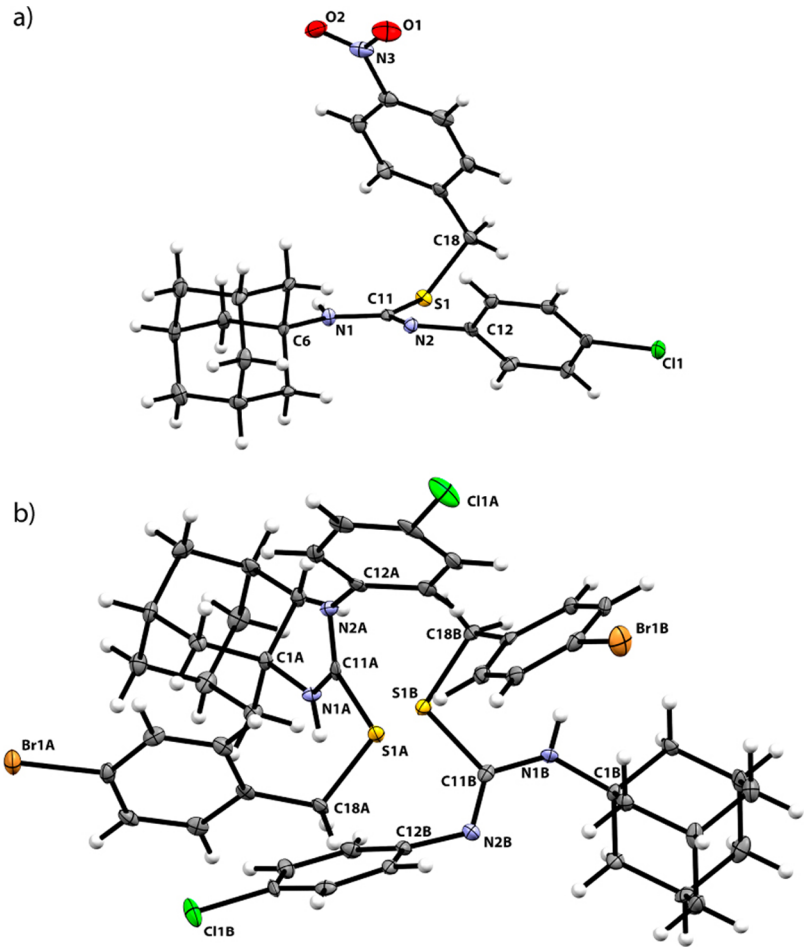

Figure 2. Ortep diagrams at 50% probability for the asymmetric units of compounds **1** (a) and **2** (b) with the numbering scheme for selected atoms. Atom color code: C (gray), H (white), O (red), N (blue), S (yellow), Cl (green), and Br (orange).

Table 2. Selected Bond Lengths and Angles in the Carbamimidothioate Group

compound **1**		compound **2A**		compound **2B**	
		bond distances (Å)			
S(1)−C(11)	1.810(5)	S(1A)−C(11A)	1.811(3)	S(1B)−C(11B)	1.808(3)
S(1)−C(18)	1.819(5)	S(1A)−C(18A)	1.822(3)	S(1B)−C(18B)	1.821(3)
N(1)−C(11)	1.359(6)	N(1A)−C(11A)	1.353(4)	N(1B)−C(11B)	1.352(4)
N(2)−C(11)	1.277(6)	N(2A)−C(11A)	1.274(4)	N(2B)−C(11B)	1.278(4)
N(1)−C(6)	1.475(6)	N(1A)−C(1A)	1.476(4)	N(1B)−C(1B)	1.480(4)
N(2)−C(12)	1.404(6)	N(2A)−C(12A)	1.409(4)	N(2B)−C(12B)	1.411(4)
		bond angles (°)			
C(11)−S(1)−C(18)	101.4(2)	C(11A)−S(1A)−C(18A)	101.32(14)	C(11B)−S(1B)−C(18B)	101.56(14)
C(11)−N(1)−C(6)	127.1(4)	C(11A)−N(1A)−C(1A)	127.9(3)	C(11B)−N(1B)−C(1B)	127.7(3)
C(11)−N(2)−C(12)	125.6(4)	C(11A)−N(2A)−C(12A)	121.0(2)	C(11B)−N(2B)−C(12B)	120.8(3)

separated by the nature of the interaction (electrostatic, polarization, dispersion, and repulsion components). The most energetic interactions for **1** are shown in Figure 6. Interestingly, the electrostatic component in the interaction energies calculated for the red and green highlighted molecules in Figure 6 is higher than that observed for the rest due to the formation of nonclassical C−H···S and nitro-nitro interactions, as described in Figure 4a.

To understand the nature of the interaction energies, energy frameworks depicting the Coulombic, dispersion, and total energy distribution within the lattice were constructed for compound 1 and molecules A and B in compound 2 and are shown in Figures S5 and S6, respectively. As expected from the high percentage of H···H interactions in the surface in both compounds, the dispersion contribution is the most significant toward the total energy within the lattice. In the case of compound 2, no pair interaction showed a significant electrostatic component toward the total energy for that pair.

2.3. Electronic Spectra. UV−vis absorption spectra of compounds 1 and 2 in methanol are shown in Figure 7a,b, respectively. Both exhibit ultraviolet absorption bands below 350 nm, although the spectral profile of 2 is somewhat shifted toward lower wavelengths. To gain further insights into the light absorption process, single-point TD-DFT (CAM-B3LYP)

https://doi.org/10.1021/acsomega.3c01469
ACS Omega 2023, 8, 13465−13477

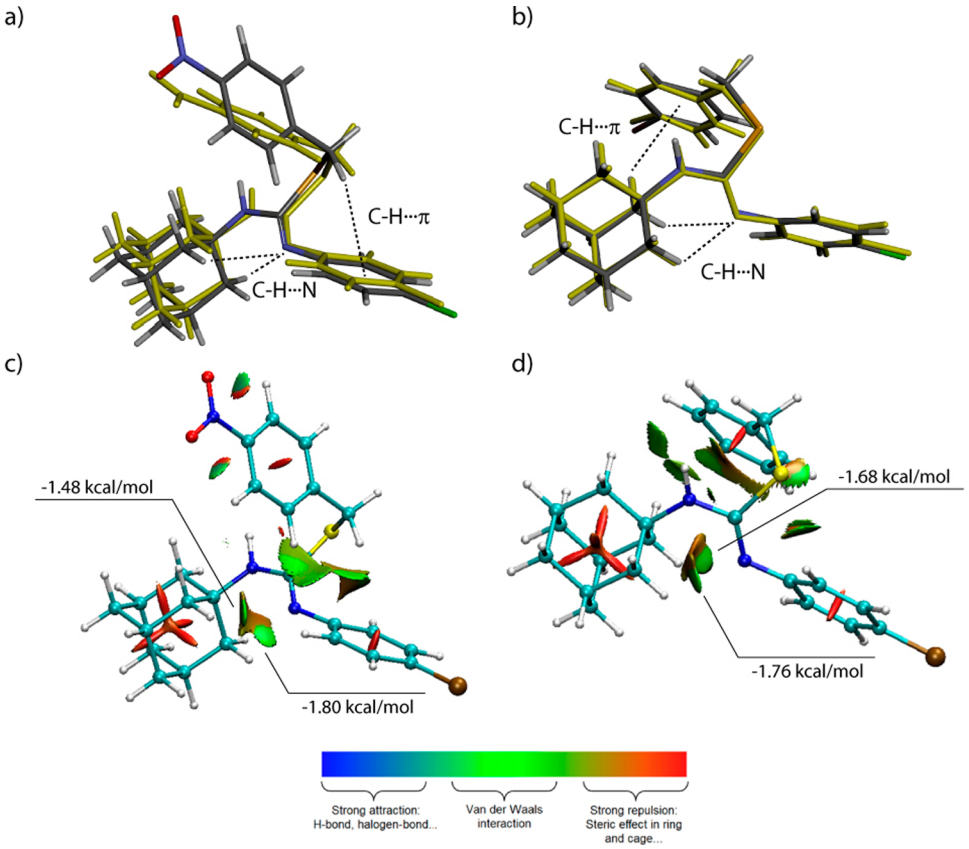

Figure 3. DFT-optimized geometries of **1** (a) and **2** (b) at the B3LYP/6-31+G(d,p) level of theory. Crystal structures are shown superimposed in yellow. Atom color code: C (gray), H (white), O (red), N (blue), S (yellow), Cl (green), Br (brown). Intramolecular interactions are represented as dashed lines. The weak interactions within the optimized geometries are depicted in (c) and (d), together with the estimated binding energies for the intramolecular H-bonds.

calculations were carried out on the DFT-optimized structures in a methanolic media (shown as dashed lines in Figure 7a,b. From that information, the electron density difference maps (EDDM) associated with the most probable electronic transitions were rendered. The latter are depicted in Figure 8c,d and indicate how the electron density changes during light absorption, moving from purple to cyan zones.

The electronic spectrum of compound 1 shows one broad band with a maximum at 249 nm and three shoulders at 306, 285, and 225 nm (Figure 7a). According to the computational model, the band centered at λ = 306 nm is brought about mainly by a $\pi \rightarrow \pi^*$ electronic transition from the HOMO to LUMO (63% contribution). The EDDM surface (Figure 7c) reveals that this transition is associated with a shift of the electron density from the chlorophenyl moiety to the nitro group. The experimental absorption band at 285 nm is computationally predicted to involve mostly a $\pi \rightarrow \pi^*$ HOMO-1 → LUMO electronic promotion (38% contribution). In this case, however, the electron density flows from the chlorophenyl and carbamimidothioate moieties to the nitro group. The most intense band, located at λ_{max} = 249 nm, is comprised by a main $\pi \rightarrow \pi^*$ electronic promotion between the HOMO and LUMO+1 (80% contribution), giving rise to an electron density shift from the carbamimidothioate moiety to the nitrobenzyl group. Lastly, the fourth band at about 225 nm is ascribed to a large number of different electronic transitions, being the most important the one involving the HOMO-2 → LUMO+1 promotion (18% contribution). The EDDM analysis suggests that the electrons flow from the chlorophenyl carbon ring and the carbamimidothioate moiety to the nitrobenzyl group and chlorine atom, respectively. Interestingly, even though the aliphatic adamantyl group does not usually contribute to UV−vis absorption bands, during this electronic promotion, there is a 7% increment of electron density around this group (Figure 7c).

The absorption spectrum of compound 2 also exhibits one broad band, centered at around 236 nm and with a shoulder near 289 nm (Figure 7b). The TD-DFT simulation suggests that the shoulder is ascribed to a $\pi \rightarrow \pi^*$ electronic transition, with contributions of HOMO → LUMO+1 (75%) and HOMO → LUMO (11%) electron promotions. During the light absorption associated with this band (289 nm), the electron density is transferred from the carbamimidothioate group toward the bromobenzyl ring, along with an electronic shift within the chlorophenyl carbon ring (Figure 8d). The second and most intense band (λ_{max} = 236 nm) is computationally predicted to be brought about by several electronic promotions. The most important one is associated with a $\pi \rightarrow \pi^*$ HOMO-1 → LUMO transition (43% contribution), corresponding to a complex displacement of the electron density, involving internal shifts within the carbamimidothioate, bromobenzyl, and chlorophenyl groups (Figure 8d). The adamantyl group does not contribute to the registered absorption bands. Finally, it is worth pointing out that, in comparison to 1, the LUMO of 2 is destabilized by 2.13 eV. This is the electronic basis behind the fact that the 2 spectral profile is shifted toward lower wavelengths.

https://doi.org/10.1021/acsomega.3c01469
ACS Omega 2023, 8, 13465−13477

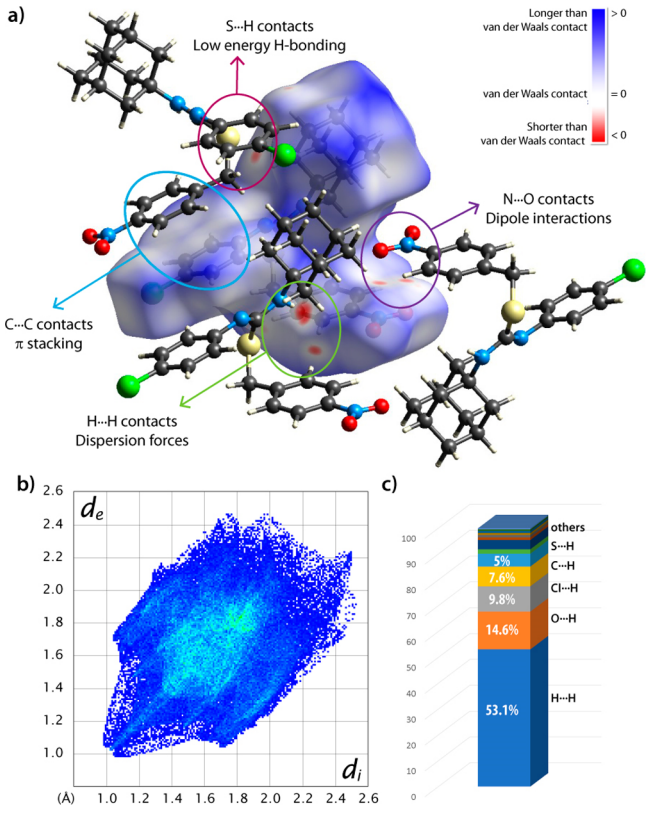

Figure 4. Intermolecular interactions analysis for **1**. (a) d_{norm} mapped within the Hirshfeld surface, adjacent molecules and intermolecular interactions are highlighted, (b) 2D fingerprint plot, and (c) contact percentage distribution; atoms involved in contacts with contributions higher than 5% are shown.

2.4. Infrared Spectra. Solid-state infrared spectroscopy was employed to structurally characterize the presented compounds. The use of computational tools to aid in the assignment of vibrational modes will be useful for future research in similar compounds. Experimental and calculated spectral profiles for compounds **1** and **2** are shown in Figure 8. Calculated spectra were simulated at the B3LYP/6-31+G(d,p) level of theory. The results were in-depth analyzed on the basis of the potential energy distribution [PED; Tables S3 and S4) in the Supporting Information]. Although calculations were performed in the gas phase, similarity overlay with the determined crystal structures is over 90% (0.91 for compound **1** and 0.94 for compound **2**, evidencing the high performance of the methods used at simulating the structural features of the molecules. Bigger shifts between calculated and experimental values are observed for vibrational modes containing the most exposed H atoms, i.e., those participating in intermolecular H-bonding.

The presence of the adamantyl substituent in both compounds can be corroborated by the absorption bands corresponding to vibrations involving aliphatic C−H and C−C bonds. For instance, aliphatic C−H stretching is registered as strong peaks in the 2950−2900 cm^{-1} range for **1** and 2911−2850 cm^{-1} for **2**. Similar results have been reported for structurally related compounds.[25,35,36] Bending modes corresponding to the CH_2 groups are found between 1480 cm^{-1} for both compounds, in line with previous evidence in related systems where these bands appear between 1400 and 1514 cm^{-1} depending on the substituents.[25,37,38] Wagging, twisting, and rocking normal modes (τ and δ in Tables S3 and S4 in the Supporting Information) are distributed along the 1360−1090 cm^{-1} range, as partial contributors to the observed bands. Asymmetric C−C stretching appears at 943 cm^{-1} for both complexes, whereas symmetric C−C stretching is assigned to 807 and 803 cm^{-1} for **1** and **2**, respectively. The fact that they are virtually equivalent evidences that these vibrations are not affected by either the substituents or the intermolecular interactions they participate in.

The carbamimidothioate moiety in the registered spectra can be recognized by the presence of the characteristic strong band at 3425 and 3441 cm^{-1}, for **1** and **2**, respectively. This is in accordance to previously studied compounds containing an adamantyl-*N*′-methylenacetohydrazide fragment, where N−H stretching frequencies appear at 3445 cm^{-1}.[25] Although this band is theoretically predicted at 3622 (**1**) and 3649 (**2**) cm^{-1}, the difference can be explained by the fact that the theoretical model, being in the gas phase and considering an isolated molecule, does not account for intermolecular interactions.

The sharp and intense peaks corresponding to N−C and C−C bond stretching are also characteristic of the carbamimidothioate group, appearing at 1629, 1310, 1151, 1009, and 943 for **1** and 1615, 1301, 1156, and 1068 cm^{-1} for **2**, while predicted between 1700 and 930 cm^{-1} for both compounds.[38]

The infrared spectra of the studied compounds display characteristic bands for benzyl and phenyl groups. For instance, aromatic C−C stretching bands are situated at 1583, 1520, 1346, 1091, and 1009 cm^{-1} for **1** and 1582, 1421, 1301, 1191, and 1068 cm^{-1} for **2**, as seen in previously reported examples.[39] As for the C−S stretching mode, it appears highly coupled with the C−Cl stretching in both compounds at 558 (**1**) and 554 (**2**) cm^{-1}, in agreement with the literature.[25]

The presence of the nitro group in **1** is corroborated by the antisymmetric N−O stretching at 1583 and 1520 cm^{-1}, as well as the symmetric N−O stretching at 1346 cm^{-1}. These are within the expected positions based on previous reports.[40,41] Also, the N−O antisymmetric stretching appears at 1504 cm^{-1}, whereas the symmetric stretching appears at 1452 cm^{-1} and at 1333 cm^{-1} (N−O symmetric stretching). Moreover, a sharp and intense peak centered at 733 cm^{-1} is also ascribed to the in-plane O−N−O bending. These wavenumbers are comparable with the ones reported in the literature: ν_{asym}(N−O) = 1530 cm^{-1}, ν_{sym}(N−O) = 1350 cm^{-1}, and δ(O−N−O) = 734 cm^{-1}.[40,41]

3. BIOLOGICAL ACTIVITIES

3.1. In Vitro Antimicrobial Activity. The in vitro growth inhibitory activity of compounds **1** and **2** against the standard bacterial strains of the American type culture collection ATCC, namely, *Staphylococcus aureus* ATCC 6571, *Bacillus subtilis* ATCC 5256, *Micrococcus luteus* ATCC 27141 (Gram-positive bacteria), *Escherichia coli* ATCC 8726, *Pseudomonas aeruginosa* ATCC 27853 (Gram-negative bacteria), and the yeast-like pathogenic fungus *Candida albicans* MTCC 227 was evaluated. The primary screening was carried out using the semi-quantitative agar-disc diffusion method with the Müller−Hinton agar medium.[42] The results of the preliminary antimicrobial screening of compounds **1**, **2** (200 μg/disc), the antibacterial antibiotics Gentamicin sulfate, Ampicillin trihydrate, and the antifungal drug Clotrimazole (100 μg/disc) are outlined in Table 3.

https://doi.org/10.1021/acsomega.3c01469
ACS Omega 2023, 8, 13465−13477

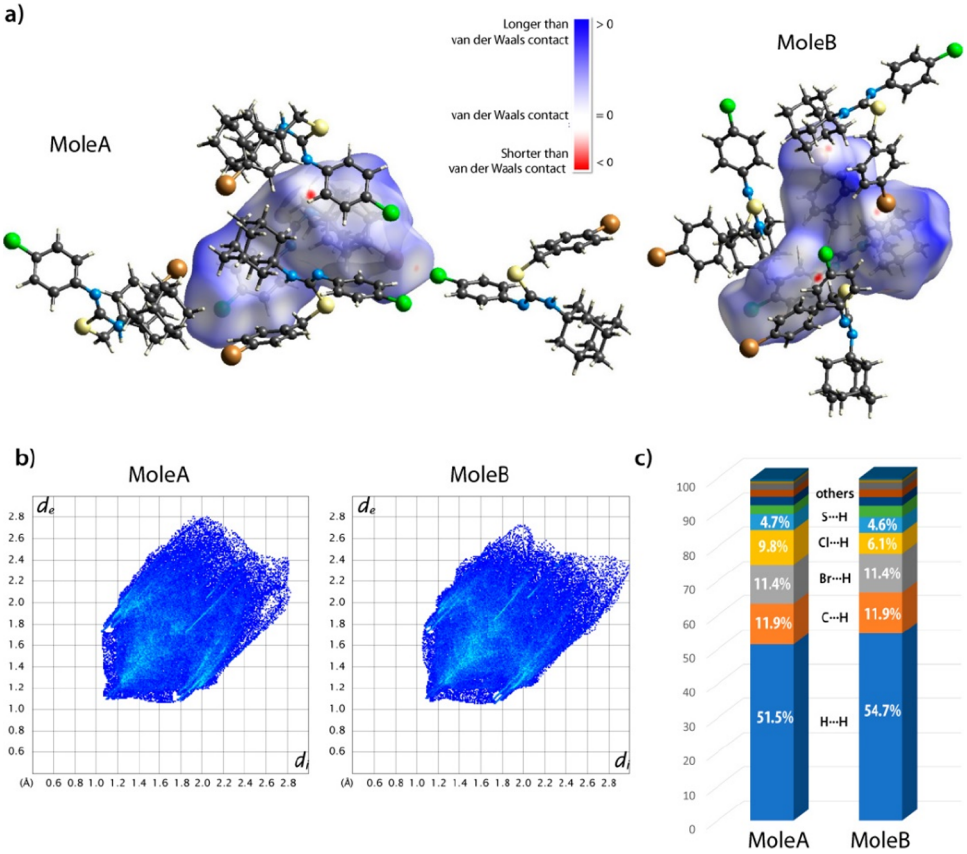

Figure 5. Intermolecular interactions analysis for **2**. (a) d_{norm} mapped within the Hirshfeld surface and adjacent molecules for the symmetrically independent A and B in **2**; (b) 2D fingerprint plot; (c) contact percentage distribution, and atoms involved in contacts with contributions lower than 4% are omitted.

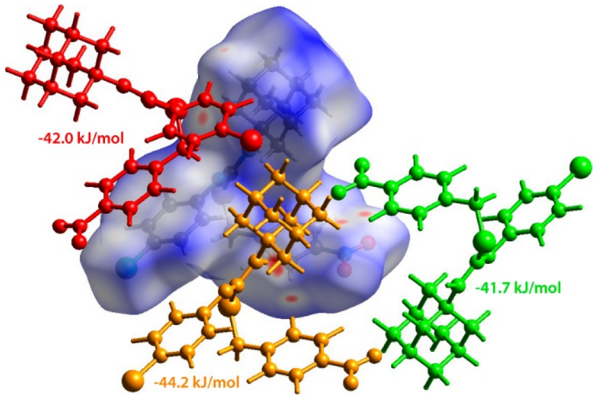

Figure 6. Calculated pair lattice energy results. Molecules are color coded as a function of symmetry and energy involved.

As evident from Table 3, compounds **1** and **2** exhibited potent antibacterial activity against all the tested Gram-positive bacterial strains and *Escherichia coli* (growth inhibition zones ≥18 mm). In addition, the nitrobenzyl analogue **1** displayed moderate inhibitory activity against *Pseudomonas aeruginosa* and the pathogenic fungus *Candida albicans* (growth inhibition zones 14−17 mm). The bromobenzyl analogue **2** showed moderate activity against *Candida albicans* and retained weak activity against *Pseudomonas aeruginosa* (growth inhibition zone 10−13 mm).

The minimal inhibitory concentration (MIC) of compounds **1** and **2** was determined against the same microorganism used in the preliminary screening using the micro-dilution susceptibility method in Müller−Hinton broth.[43] The values of the MIC for compounds **1**, **2** and the reference antimicrobial drugs Gentamicin sulfate, Ampicillin trihydrate, and Clotrimazole (Table 3) were almost consistent with the results obtained in the preliminary screening.

3.2. In Vitro Antiproliferative Activity. The in vitro antiproliferative activity of compounds **1** and **2** was assessed against five human tumor cell lines, namely, PC-3 (human prostate cancer), HepG-2 (hepatocellular carcinoma), HCT-116 (colorectal carcinoma), MCF-7 (mammary gland breast cancer), and HeLa (epithelioid carcinoma) using the 3-[4,5-dimethylthiazoyl-2-yl]-2,5-diphenyltetrazolium bromide (MTT) colorimetric assay.[44] The results of in vitro antiproliferative activity of compounds **1**, **2**, and the anticancer drug doxorubicin are shown in Table 4.

The antiproliferative activity results revealed that the compound 4-bromobenzyl analogue **2** exhibited good antiproliferative activity with IC_{50} < 25 μM against PC-3, HepG-2, MCF-7, and HeLa cell lines and moderate activity (IC_{50}: 25−50 μM) against the HCT-116 cell line. Meanwhile, the 4-nitrobenzyl analogue **1** only retained moderate activity against the tested cell lines. In general, the antiproliferative activity of the compounds against MCF-7, HeLa, and, to a lesser extent, HepG-2 is higher than the activity against PC-3 and HCT-116 cell lines.

https://doi.org/10.1021/acsomega.3c01469
ACS Omega 2023, 8, 13465−13477

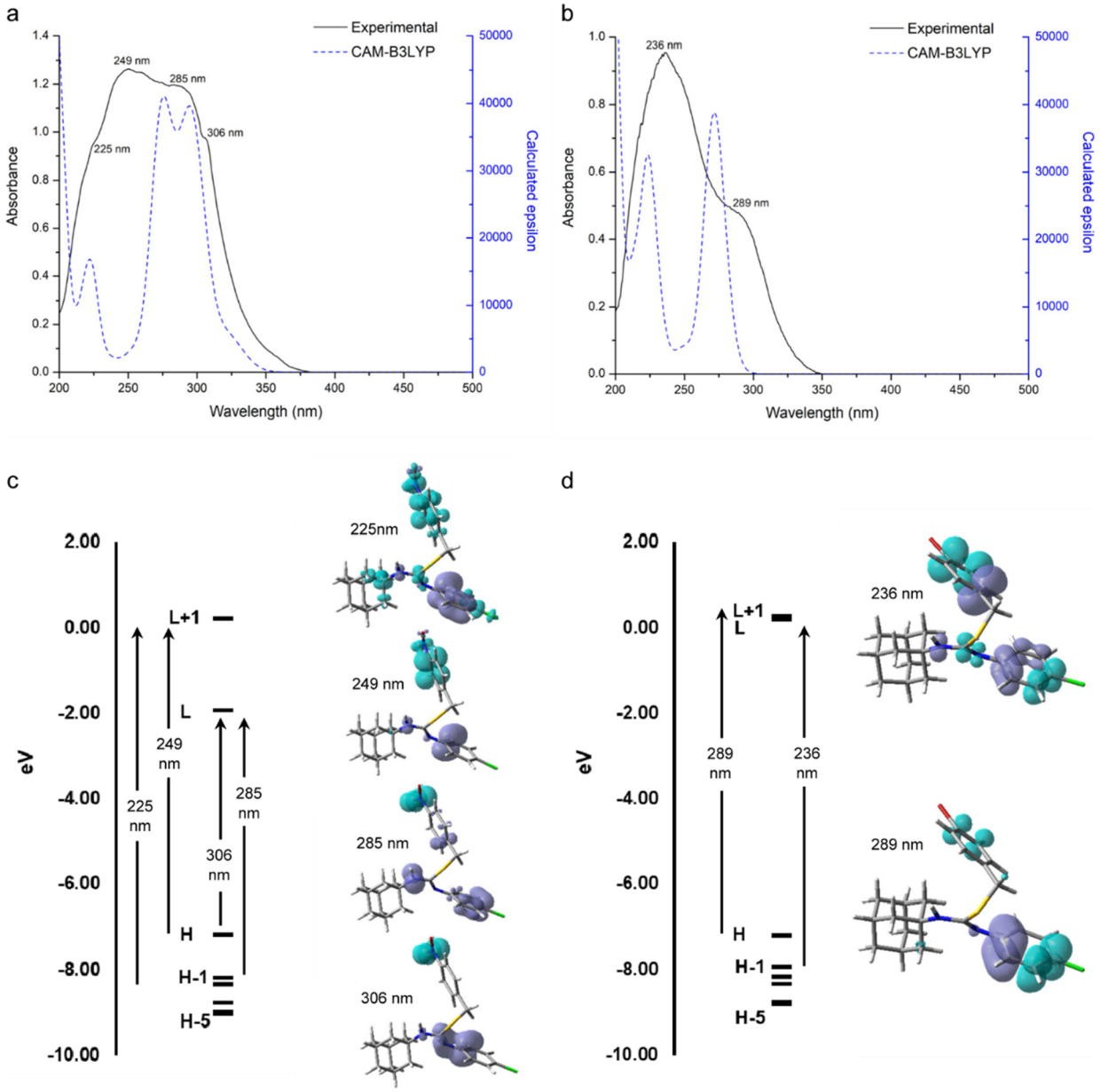

Figure 7. UV−vis spectra of a 10 μg/mL methanolic solution of compounds **1** (a) and **2** (b). Experimental and calculated spectra (CAM-B3LYP/6-311+G(d,p) − SMD) are depicted as solid and dashed lines, respectively. For the theoretical spectra, the half-width at half height is 0.15 eV. In (c,d), the molecular orbitals involved in the different electronic transitions and their energies are shown for both systems. The electron density difference maps (EDDM; isovalue = 0.002) associated with the electronic transitions are also depicted. The electron density changes from purple to cyan upon light absorption. Color code: C (gray), H (white), O (red), N (blue), S (yellow), Cl (green), Br (Brown). H = HOMO, L = LUMO.

4. CONCLUSIONS

Two novel adamantane-linked isothiourea derivatives, **1** and **2**, were successfully obtained in good yields and high purity. Both compounds were chemically and structurally characterized by a combination of experimental and computational techniques. Single-crystal X-ray diffraction, in conjunction with infrared and electronic spectroscopy, provides a clear picture of the molecular structure and the intermolecular interactions at play. This information will come in handy to aid the characterization of similar systems developed in the future.

Both compounds exhibited marked chemotherapeutic activities. Regarding the antimicrobial activity, the compounds exhibit similar comparable MIC values than reference drugs (Gentamicin sulfate and Ampicillin trihydrate) against *Bacillus subtilis* and *Micrococcus luteus*. As far as the anti-proliferative activity is concerned, the studied compounds are less active than Doxorubicin. However, the 4-bromobenzyl analogue exhibits high antiproliferative activity with IC_{50} < 25 μM against PC-3, HepG-2, MCF-7, and HeLa cell lines and moderate activity (IC_{50}: 25−50 μM) against the HCT-116 cell line. In this sense, compounds **1** and **2** constitute good candidates as antimicrobial and anticancer agents, giving proof that the adamantyl/isothiourea combined scaffold opens up a new avenue in the quest for potent chemotherapeutic agents.

5. MATERIALS AND METHODS

5.1. Synthesis and Crystallization. The appropriate arylmethy bromide (2.0 mmol) and anhydrous potassium carbonate (277 mg, 2.0 mmol) were added to a solution of 1-

https://doi.org/10.1021/acsomega.3c01469
ACS Omega 2023, 8, 13465−13477

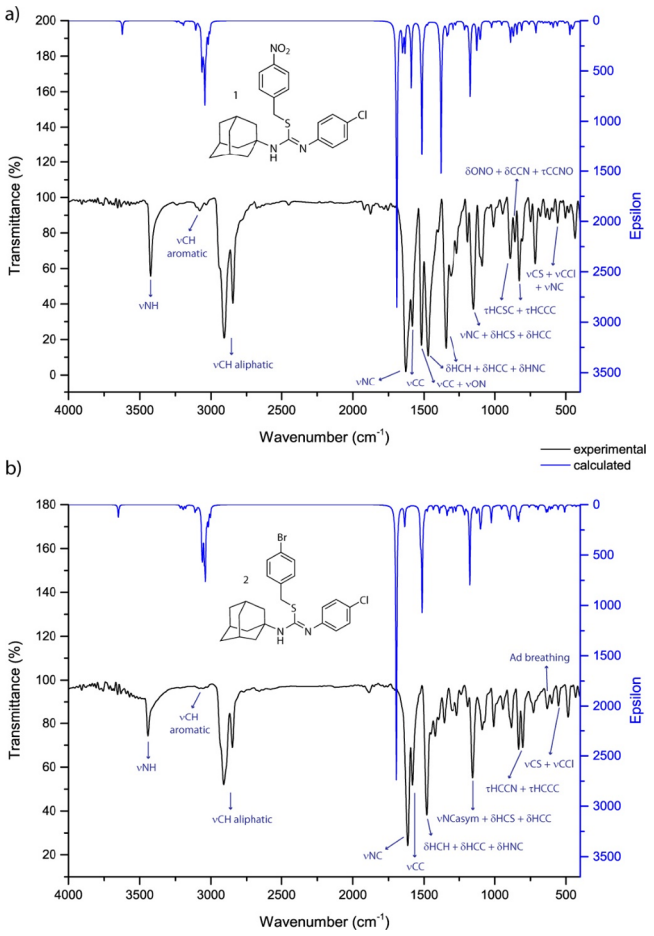

Figure 8. Experimental vs calculated FTIR for compounds **1** (a) and **2** (b). Selected assigned bands are depicted with arrows.

(adamantan-1-yl)-3-(4-chlorophenyl)thiourea (642 mg, 2.0 mmol), in acetone (10 mL), and the mixture was heated under reflux with stirring for 3 h. The solvent was then distilled off in vacuo, and the residue was washed with water, dried, and crystallized from ethanol to yield the target products **1** and **2**. Single crystals suitable for X-ray diffraction were obtained by slow evaporation of a solution of each compound in ethanol−chloroform (1:1, v/v) held at room temperature.

*5.1.1. 4-Nitrobenzyl (Z)-N-(Adamantan-1-yl)-N′-(4-chlorophenyl)carbamimidothioate (**1**).* Colorless block crystals; yield (821 mg, 90%); m.p. 123−125 °C. Analysis Calcd. for $C_{24}H_{26}ClN_3O_2S$: C, 63.22; H, 5.75; N, 9.22; S, 7.03%. Found: C, 63.16; H, 5.80; N, 9.20; S, 7.01%. ^{1}H NMR ($CDCl_3$, 500.13 MHz): δ 1.52−1.68 (m, 6H, Adamantane-H), 1.98 (s, 6H, Adamantane-H), 2.05 (s, 3H, Adamantane-H), 4.26 (s, 2H, benzylic CH_2), 6.84−6.86 (m, 3H, Ar−H & NH), 7.20−7.29 (m, 2H, Ar−H), 7.36 (d, 2H, Ar−H, J = 7.0 Hz), 8.18 (d, 2H, Ar−H, J = 7.5 Hz). ^{13}C NMR ($CDCl_3$, 125.76 MHz): δ 29.51, 36.25, 41.79, 53.65 (Adamantane-C), 35.95 (benzylic CH_2), 123.24, 123.79, 129.01, 129.58, 132.25, 144.35, 146.05, 148.0 (Ar−H), 153.66 (C═N). ESI-MS, m/z: 456.4 $[M + H, 100\%]^+$, 458.4 $[M + 2 + H, 36\%]^+$.

*5.1.2. 4-Bromobenzyl (Z)-N-(Adamantan-1-yl)-N′-(4-chlorophenyl)carbamimidothioate (**2**).* Colorless block crystals; yield (784 mg, 80%); m.p. 102−104 °C. Analysis Calcd. for $C_{24}H_{26}BrClN_2S$: C, 58.84; H, 5.35; N, 5.72; S, 6.54%. Found: C, 58.65; H, 5.40; N, 5.67; S, 6.48%. ^{1}H NMR ($CDCl_3$, 700.17 MHz): δ 1.64−1.66 (m, 6H, Adamantane-H), 1.98 (s, 6H, Adamantane-H), 2.12 (s, 3H, Adamantane-H), 4.23 (s, 2H, benzylic CH_2), 6.86−7.12 (m, 3H, Ar−H & NH), 7.22−7.26 (m, 4H, Ar−H), 7.36 (d, 2H, Ar−H, J = 7.0 Hz). ^{13}C NMR ($CDCl_3$, 176.08 MHz): δ 28.90, 35.95, 41.12, 52.88 (Adamantane-C), 36.44 (benzylic CH_2), 120.06, 123.80, 129.56, 130.04, 130.98, 133.14, 137.88, 148.06 (Ar−C), 151.98 (C═N). ESI-MS, m/z: 498.4 $[M + H, 44\%]^+$, 499.4 $[M + 1 + H, 38\%]^+$, 500.4 $[M + 2 + H, 100]^+$.

5.2. Single Crystal X-ray Diffraction Measurements. Suitable single crystals were used for diffraction measurements on Bruker APEX-II CCD (compound **1**) and D8 Venture (compound **2**) diffractometers using a single wavelength X-ray source (MoK_α radiation: λ = 0.71073 Å). Measurement strategy determination and data collection were performed on Bruker APEX2 software.[45] SAINT[46] was used for cell refinement and data reduction; the structure was solved by direct methods with SHELXLS-97,[47] and multi-scan absorption correction was applied using Bruker SADABS.[48] SHELXL-2014[49] was used for structure refinement by full-matrix least-squares minimization on F^2.

All non-hydrogen atoms were refined using anisotropic displacement parameters. Hydrogen atoms were geometrically positioned and refined isotropically using the *riding model*, thermal parameters set at 1.2 times the $U_{iso,eq}$ of the preceding C and N atoms. Molecular graphics were prepared using Mercury.[50] A detailed summary of crystallographic data including experimental details and refinement results is available in Table 1.

Crystallographic data are deposited on the CCDC under deposition numbers 1906754 and 2211104, for compounds **1** and **2**, respectively. CIF files can be accessed free of charge

Table 3. Antimicrobial Activity of Compounds 1, 2 (200 μg/8 mm Disc), the Broad Spectrum Antibacterial Drugs Gentamicin Sulfate (100 μg/8 mm Disc), Ampicillin Trihydrate (100 μg/8 mm Disc) and the Antifungal Drug Clotrimazole (100 μg/8 mm Disc) against *Staphylococcus aureus* ATCC 6571 (*SA*), *Bacillus subtilis* ATCC 5256 (*BS*), *Micrococcus luteus* ATCC 27141 (*ML*), *Escherichia coli* ATCC 8726 (*EC*), *Pseudomonas aeruginosa* ATCC 27853 (*PA*), and the Yeast-like Pathogenic Fungus *Candida albicans* MTCC 227 (*CA*)

compound	diameter of growth inhibition zone (mm)[a]					
	SA	*BS*	*ML*	*EC*	*PA*	*CA*
1	24 (1)	25 (1)	22 (2)	19 (4)	16	15
2	22 (8)	24 (2)	19 (2)	19 (8)	13	14
gentamicin sulfate	27 (1)	26 (2)	20 (2)	22 (0.5)	21 (0.5)	NT
ampicillin trihydrate	22 (2)	23 (1)	20 (2)	16 (8)	18 (8)	NT
clotrimazole	NT	NT	NT	NT	NT	21 (4)

[a]Figures shown in parentheses represent the MIC values (μg/mL), NT: not tested.

https://doi.org/10.1021/acsomega.3c01469
ACS Omega 2023, 8, 13465−13477

Table 4. In Vitro Antiproliferative Activity of Compounds 1, 2, and the Anticancer Drug Doxorubicin toward Human Prostate Cancer (PC-3), Hepatocellular Carcinoma (HepG-2), Colorectal Carcinoma (HCT-116), Mammary Gland Breast Cancer (MCF-7), and Epithelioid Carcinoma (HeLa) Cell Lines

compound	IC_{50} (μM)[a]				
	PC-3	HepG-2	HCT-116	MCF-7	HeLa
1	47.24 ± 1.6	36.12 ± 3.4	46.11 ± 3.5	32.12 ± 2.9	27.52 ± 2.7
2	22.22 ± 3.1	19.16 ± 1.4	30.0 ± 3.2	15.16 ± 2.3	22.10 ± 2.1
doxorubicin	8.87 ± 0.6	4.50 ± 0.2	5.23 ± 0.3	4.17 ± 0.2	5.57 ± 0.4

[a]IC_{50} values presented as the mean ± SD of three separate determinations.

through the access structure applet in the CCDC webpage (https://www.ccdc.cam.ac.uk/structures).

5.3. Hirshfeld Surface Analysis. Intermolecular interactions were further analyzed by means of Hirshfeld surface analysis and 2D plots of normalized contact distances. Both were constructed using CrystalExplorer17.5.[51−53] The normalized contact distance (d_{norm}) is defined as follows:

$$d_{norm} = \frac{d_i - r_i^{vdW}}{r_i^{vdW}} + \frac{d_e - r_e^{vdW}}{r_e^{vdW}}$$

where d_e and d_i represent the distances from a point on the surface to the nearest nucleus outside (d_e) and inside (d_i) the surface, respectively, and r^{vdW} corresponds to the van der Waals (vdW) radii of the atoms involved. The 2D fingerprint plot is a graph of d_e vs d_i distances within the surface (and their frequency) which provides quantitative information on the type of intermolecular interactions present in the crystal.[54] To further understand the nature of the energies governing crystal packing, lattice energies were computed with the CE-B3LYP/6-31G(d,p) model within Tonto embedded in Crystal Explorer. Based on the position of the molecules in the lattice, the energy between unique molecular pairs within a 3.8 radius was estimated as a sum of the electrostatic, polarization, dispersion, and repulsion energies.[55]

5.4. Computational Calculations. To model the vibrational spectra, X-ray structures were employed as starting geometries for compounds **1** and **2** and were fully optimized by means of the density functional theory method (DFT)[56] without symmetry constraints, employing the B3LYP functional,[57] and the 6-31+G** basis set.[58] Gaussian 09 software[59] was used to perform calculations in the gas phase with an ultrafine integration grid. Potential Energy Distribution (PED) analyses were performed on the calculated vibrational modes using VEDA 4 software[60] in order to assign the corresponding vibrational modes. A scale factor of 0.964 was applied to computed vibrational frequencies.[61]

A topology analysis of the electron density of compounds **1** and **2** was performed with the program Multiwfn (version 3.7),[62] starting from the gas-phase optimum geometries. From this data, the weak interactions were identified and analyzed by means of the noncovalent interaction (NCI) method.[34] In detail, the $sign(\lambda_2)\rho$ products were represented with different colors and mapped on a reduced density gradient isosurface (isovalue = 0.5; λ_2 = second largest eigenvalue of the Hessian matrix of electron density; ρ = electron density). The weak interactions were then represented with different colors: H-bonds (blue), van der Waals (green), and steric repulsion (red). The H-bond binding energy was estimated from the electron density at the bond critical point (ρ_{BCP}), according to Emamian et al.[63]

To model the electronic spectra in methanol for compounds **1** and **2**, the X-ray crystallographic structures of both molecules were pre-optimized in solution by molecular mechanics, employing the MMFF94X forcefield (energy gradient = 0.01 kcal/mol/Å^3), as implemented in MOE.[64] The solvent was modeled by means of the Generalized Born model (ε = 33.1). To explore the conformational space, a search on the potential energy surface was carried out with the LowModeMD method,[65] using the same forcefield and solvation method, without cut-offs, and with an RMS gradient = 0.005 kcal/mol/Å^3 (rejection limit = 100; RMSD limit = 0.25 Å; energy window = 7 kcal/mol; iteration limit = 10,000). There were 12 conformers found for **1** and 25 for **2**. The most stable conformers for both compounds were re-optimized in solution by DFT (B3LYP/6-31+G**). The influence of the solvent was simulated by an IEFPCM method (implicit solvation), with radii and nonelectrostatic terms from Truhlar and coworkers' SMD solvation model.[66] Finally, single-point TD-DFT calculations were carried out on the optimum geometries to simulate the UV−visible light absorption process.[56] Singlet-to-singlet electronic transitions were considered and their vertical energies were computed in methanol at the CAM-B3LYP-SMD/6-311+G(d,p) level of theory.[67] An in-depth analysis of the light absorption mechanism was carried out with the aid of GaussSum 3.0 program.[68] The EDDM and the molecular orbitals related to the most probable electronic transitions were computed.

In all cases, the analytically computed Hessian matrix presented only real vibrational frequencies, verifying the nature of the stationary point. Gaussview 6.0,[69] VMD 1.9.3,[70] and Discovery Studio Visualizer[71] were used to prepare the graphic material.

■ ASSOCIATED CONTENT

Supporting Information

The Supporting Information is available free of charge at https://pubs.acs.org/doi/10.1021/acsomega.3c01469.

Mogul search histogram for the C11−N2 bond in compound **1**; Mogul search histogram for the C11−N1 bond in compound **1**; Mogul search histogram for the C11−N2 bond in compound **2**; Mogul search histogram for the C11−N1 bond in compound **2**; energy frameworks for compound **1**; energy frameworks for molecules A and B in compound **2**; lattice energy calculations for compound **1**; lattice energy calculations for molecules A and B in compound **2**; experimental and calculated FTIR results summary for compound **1**; and experimental and calculated FTIR results summary for compound **2** (PDF)

https://doi.org/10.1021/acsomega.3c01469
ACS Omega 2023, 8, 13465−13477

AUTHOR INFORMATION

Corresponding Authors

Natalia Alvarez − *Química Inorgánica, Facultad de Química, Universidad de la República, Montevideo 11800, Uruguay*; Email: nalvarez@fq.edu.uy

Ali A. El-Emam − *Department of Medicinal Chemistry, Faculty of Pharmacy, Mansoura University, Mansoura 35516, Egypt*; orcid.org/0000-0002-9325-9497; Email: elemam5@hotmail.com

Authors

Fatmah A. M. Al-Omary − *Department of Pharmaceutical Chemistry, College of Pharmacy, King Saud University, Riyadh 11451, Saudi Arabia*

Lamees S. Al-Rasheed − *Department of Pharmaceutical Chemistry, College of Pharmacy, King Saud University, Riyadh 11451, Saudi Arabia*

Nicolás Veiga − *Química Inorgánica, Facultad de Química, Universidad de la República, Montevideo 11800, Uruguay*; orcid.org/0000-0001-8552-058X

Hanan M. Hassan − *Department of Pharmacology and Biochemistry, Faculty of Pharmacy, Delta University for Science and Technology, Mansoura 11152, Egypt*

Complete contact information is available at: https://pubs.acs.org/10.1021/acsomega.3c01469

Notes

The authors declare no competing financial interest.

ACKNOWLEDGMENTS

Dr. N.A. and Dr. N.V. thank PEDECIBA Química.

REFERENCES

(1) Spilovska, K.; Zemek, F.; Korabecny, J.; Nepovimova, E.; Soukup, O.; Windisch, M.; Kuca, K. Adamantane - a lead structure for drugs in clinical practice. *Curr. Med. Chem.* **2016**, *23*, 3245−3266.

(2) Wanka, L.; Iqbal, K.; Schreiner, P. R. The lipophilic bullet hits the targets: Medicinal chemistry of adamantane derivatives. *Chem. Rev.* **2013**, *113*, 3516−3604.

(3) Liu, J.; Obando, D.; Liao, V.; Lifa, T.; Codd, R. The many faces of the adamantyl group in drug design. *Eur. J. Med. Chem.* **2011**, *46*, 1949−1963.

(4) Davies, W. L.; Grunnert, R. R.; Haff, R. F.; McGahen, J. W.; Neumeyer, E. M.; Paulshock, M.; Watts, J. C.; Wood, T. R.; Hermann, E. C.; Hoffmann, C. E. Antiviral activity of 1-adamantamine (amantadine). *Science* **1964**, *144*, 862−863.

(5) Wendel, H. A.; Snyder, M. T.; Pell, S. Trial of amantadine in epidemic influenza. *Clin. Pharmacol. Ther.* **1966**, *7*, 38−43.

(6) Wingfield, W. L.; Pollack, D.; Grunert, R. R. Treatment of influenza. The therapeutic efficacy of rimantadine HCl in a naturally occurring influenza A_2 respiratory illness in man. *N. Engl. J. Med.* **1969**, *281*, 579−584.

(7) Rosenthal, K. S.; Sokol, M. S.; Ingram, R. L.; Subramanian, R.; Fort, R. C. Tromantadine: Inhibitor of early and late events in *herpes simplex* virus replication. *Antimicrob. Agents Chemother.* **1982**, *22*, 1031−1036.

(8) Protopopova, M.; Hanrahan, C.; Nikonenko, B.; Samala, R.; Chen, P.; Gearhart, J.; Einck, L.; Nacy, C. A. Identification of a new antitubercular drug candidate, SQ109, from a combinatorial library of 1,2-ethylenediamines. *J. Antimicrob. Chemother.* **2005**, *56*, 968−974.

(9) Bogatcheva, E.; Hanrahan, C.; Chen, P.; Gearhart, J.; Sacksteder, K.; Einck, L.; Nacy, C.; Protopopova, M. Discovery of dipiperidines as new antitubercular agents. *Bioorg. Med. Chem. Lett.* **2010**, *20*, 201−205.

(10) Long, J.; Manchandia, T.; Ban, K.; Gao, S.; Miller, C.; Chandra, J. Adaphostin cytoxicity in glioblastoma cells is ROS-dependent and is accompanied by upregulation of heme oxygenase-1. *Cancer Chemother. Pharmacol.* **2007**, *59*, 527−535.

(11) Lorenzo, P.; Alvarez, R.; Ortiz, M. A.; Alvarez, S.; Piedrafita, F. J.; de Lera, A. R. Inhibition of IκB kinase-β and anticancer activities of novel chalcone adamantyl arotinoids. *J. Med. Chem.* **2008**, *51*, 5431−5440.

(12) Han, T.; Goralski, M.; Capota, E.; Padrick, S. B.; Kim, J.; Xie, Y.; Nijhawan, D. The antitumor toxin CD437 is a direct inhibitor of DNA polymerase α. *Nat. Chem. Biol.* **2016**, *12*, 511−515.

(13) Dai, L.; Smith, C. D.; Foroozesh, M.; Miele, L.; Qin, Z. The sphingosine kinase 2 inhibitor ABC294640 displays anti-non-small cell lung cancer activities *in vitro* and *in vivo*. *Int. J. Cancer* **2018**, *142*, 2153−2162.

(14) Lain, S.; Hollick, J. J.; Campbell, J.; Staples, O. D.; Higgins, M.; Aoubala, M.; McCarthy, A.; Appleyard, V.; Murray, K. E.; Baker, L.; Thompson, A.; Mathers, J.; Holland, S. J.; Stark, M. J. R.; Pass, G.; Woods, J.; Lane, D. P.; Westwood, N. J. Discovery, *In vivo* activity, and mechanism of action of a small-molecule p53 activator. *Cancer Cell* **2008**, *13*, 454−463.

(15) Koronkiewicz, M.; Romiszewska, A.; Chilmonczyk, Z.; Kazimierczuk, Z. New benzimidazole-derived isothioureas as potential antileukemic agents - studies *in vitro*. *Med. Chem.* **2015**, *11*, 364−372.

(16) Huang, X.; Huang, R.; Liao, Z.; Pan, Y.; Gou, S.; Wang, H. Synthesis and pharmacological evaluation of dehydroabietic acid thiourea derivatives containing bisphosphonate moiety as an inducer of apoptosis. *Eur. J. Med. Chem.* **2016**, *108*, 381−391.

(17) D'Cruz, O. J.; Uckun, F. M. Novel broad-spectrum thiourea non-nucleoside inhibitors for the prevention of mucosal HIV transmission. *Curr. HIV Res.* **2006**, *4*, 329−345.

(18) Thoma, G.; Streiff, M. B.; Kovarik, J.; Glickman, F.; Wagner, T.; Beerli, C.; Zerwes, H. G. Orally bioavailable isothioureas block function of the chemokine receptor CXCR4 *in vitro* and *in vivo*. *J. Med. Chem.* **2008**, *51*, 7915−7920.

(19) Joshi, S. D.; Dixit, S. R.; Kirankumar, M. N.; Aminabhavi, T. M.; Raju, K. V.; Narayan, R.; Lherbet, C.; Yang, K. S. Synthesis, antimycobacterial screening and ligand-based molecular docking studies on novel pyrrole derivatives bearing pyrazoline, isoxazole and phenyl thiourea moieties. *Eur. J. Med. Chem.* **2016**, *107*, 133−152.

(20) Verlinden, B. K.; Niemand, J.; Snyman, J.; Sharma, S. K.; Beattie, R. J.; Woster, P. M.; Birkholtz, L. M. Discovery of novel alkylated (bis)urea and (bis)thiourea polyamine analogues with potent antimalarial activities. *J. Med. Chem.* **2011**, *54*, 6624−6633.

(21) El-Emam, A. A.; Al-Deeb, O. A.; Al-Omar, M.; Lehmann, J. Synthesis, antimicrobial, and anti-HIV-1 activity of certain 5-(1-adamantyl)-2-substituted thio-1,3,4-oxadiazoles and 5-(1-adamantyl)-3-substituted aminomethyl-1,3,4-oxadiazoline-2-thiones. *Bioorg. Med. Chem.* **2004**, *12*, 5107−5113.

(22) El-Emam, A. A.; Al-Tamimi, A. M. S.; Al-Omar, M. A.; Alrashood, K. A.; Habib, E. E. Synthesis and antimicrobial activity of novel 5-(1-adamantyl)-2-aminomethyl-4-substituted-1,2,4-triazoline-3-thiones. *Eur. J. Med. Chem.* **2013**, *68*, 96−102.

(23) Hassan, H. M.; Al-Wahaibi, L. H.; Shehatou, G. S.; El-Emam, A. A. Adamantane-linked isothiourea derivatives suppress the growth of experimental hepatocellular carcinoma via inhibition of TLR4-MyD88-NF-κB signalling. *Am. J. Cancer Res.* **2021**, *11*, 350−369 PubMed ID: 33575076..

(24) Al-Wahaibi, L. H.; Hassan, H. M.; Abo-Kamar, A. M.; Ghabbour, H. A.; El-Emam, A. A. Adamantane-isothiourea hybrid derivatives: Synthesis, characterization, *in vitro* antimicrobial, and *in vivo* hypoglycemic activities. *Molecules* **2017**, *22*, 710.

(25) Al-Wahaibi, L. H.; Alvarez, N.; Blacque, O.; Veiga, N.; Al-Mutairi, A. A.; El-Emam, A. A. Synthesis and structure insights of two novel broad-spectrum antibacterial candidates based on (*E*)-*N*'-[(heteroaryl)methylene]adamantane-1-carbohydrazides. *Molecules* **2020**, *25*, 1934.

(26) El-Emam, A. A.; Kumar, E. S.; Janani, K.; Al-Wahaibi, L. H.; Blacque, O.; El-Awady, M. I.; Al-Shaalan, N. H.; Percino, M. J.;

Thamotharan, S. Quantitative assessment of the nature of non-covalent interactions in *N*-substituted-5-(adamantan-1-yl)-1,3,4-thiadiazole-2-amines: Insights from crystallographic and QTAIM analysis. *RSC Adv.* **2020**, *10*, 9840−9853.
(27) Al-Wahaibi, L. H.; Grandhi, D. S.; Tawfik, S. S.; Al-Shaalan, N. H.; Elmorsy, M. A.; El-Emam, A. A.; Percino, M. J.; Thamotharan, S. Probing the effect of halogen substituents (Br, Cl, and F) on the non-covalent interactions in 1-(adamantan-1-yl)-3-arylthiourea derivatives: A theoretical study. *ACS Omega* **2021**, *6*, 4816−4830.
(28) Al-Wahaibi, L. H.; Asokan, K. V.; Al-Shaalan, N. H.; Tawfik, S. S.; Hassan, H. M.; El-Emam, A. A.; Percino, M. J.; Thamotharan, S. Supramolecular self-assembly mediated by multiple hydrogen bonds and the importance of C−S···N chalcogen bonds in *N*′-(adamantan-2-ylidene)hydrazide derivatives. *ACS Omega* **2022**, *7*, 10608−10621.
(29) Al-Omary, F. A. M.; Chowdary Gude, N.; Al-Rasheed, L. S.; Alkahtani, H. N.; Hassan, H. M.; Al-Abdullah, E. S.; El-Emam, A. A.; Percino, M. J.; Thamotharan, S. X-ray and theoretical investigation of (*Z*)-3-(adamantan-1-yl)-1-(phenyl or 3-chlorophenyl)-*S*-(4-bromobenzyl)isothioureas: an exploration involving weak non-covalent interactions, chemotherapeutic activities and QM/MM binding energy. *J. Biomol. Struct. Dyn.* **2022**, *40*, 2530−2545.
(30) Al-Omary, F. A. M.; Ghabbour, H. A.; AlRabiah, H.; Al-Abdullah, E. S.; El-Emam, A. A. Crystal structure of 1-(adamantan-1-yl)-3-(4-chlorophenyl)thiourea, $C_{17}H_{21}ClN_2S$. *Z. Kristallogr. - New Cryst. Struct.* **2016**, *232*, 707−709.
(31) Groom, C. R.; Bruno, I. J.; Lightfoot, M. P.; Ward, S. C. The Cambridge structural database. *Acta Crystallogr., Sect. B: Struct. Sci., Cryst. Eng. Mater.* **2016**, *72*, 171−179.
(32) El-Emam, A. A.; Al-Omary, F. A. M.; Al-Rasheed, L. S.; Ghabbour, H. A.; Al-Abdullah, E. S. Crystal structure of (*Z*)-3-(adamantan-1-yl)-1-(3-chlorophenyl)-*S*-benzylisothiourea, $C_{24}H_{27}ClN_2S$. *Z. Kristallogr. - New Cryst. Struct.* **2017**, *232*, 453−456.
(33) Al-Wahaibi, L. H.; Sujay, S.; Muthu, G. G.; El-Emam, A. A.; Venkataramanan, N. S.; Al-Omary, F. A. M.; Ghabbour, H. A.; Percino, M. J.; Thamotharan, S. Theoretical investigations of two adamantane derivatives: A combined X-ray, DFT, QTAIM analysis and molecular docking. *J. Mol. Struct.* **2018**, *1159*, 233−245.
(34) Johnson, E. R.; Keinan, S.; Mori-Sánchez, P.; Contreras-García, J.; Cohen, A. Y.; Yang, W. Revealing noncovalent interactions. *J. Am. Chem. Soc.* **2010**, *132*, 6498−6506.
(35) Wiberg, K. B. Application of the pople-santry-segal CNDO method to the cyclopropylcarbinyl and cyclobutyl cation and to bicyclobutane. *Tetrahedron* **1968**, *24*, 1083−1096.
(36) Al-Wahaibi, L. H.; Sert, Y.; Ucun, F.; Al-Shaalan, N. H.; Alsfouk, A. A.; El-Emam, A. A.; Karakaya, M. Theoretical and experimental spectroscopic studies, XPS analysis, dimer interaction energies and molecular docking study of 5-(adamantan-1-yl)-*N*-methyl-1,3,4-thiadiazol-2-amine. *J. Phys. Chem. Solids* **2019**, *135*, No. 109091.
(37) El-Emam, A. A.; Al-Tamimi, A. M. S.; Al-Rashood, K. A.; Misra, H. N.; Narayan, V.; Prasad, O.; Sinha, L. Structural and spectroscopic characterization of a novel potential chemotherapeutic agent 3-(1-adamantyl)-1-{[4-(2-methoxyphenyl)piperazin-1-yl]methyl}-4-methyl-1*H*-1,2,4-triazole-5(4*H*)-thione by first principle calculations. *J. Mol. Struct.* **2012**, *1022*, 49−60.
(38) Tamer, Ö.; Avcı, D.; Atalay, Y. Quantum chemical characterization of *N*-(2-hydroxybenzylidene)acetohydrazide (HBAH): a detailed vibrational and NLO analysis. *Spectrochim. Acta, Part A* **2014**, *117*, 78−86.
(39) Varsányi, G., *Vibrational spectra of benzene derivatives*; Elsevier, 2012.
(40) Arcoria, A.; Maccarone, E.; Tomaselli, G. A. Electronic spectra and infrared characteristics of trans-2-styrylthiophene and some nitro derivatives. *Spectrochim. Acta, Part A* **1973**, *29*, 1601−1609.
(41) Feuer, H.; Savides, C.; Rao, C. N. R. The infrared spectra of the salts of nitro compounds. Characteristic frequencies of the carbonitronate group, $=C=NO_2^-$*. *Spectrochim. Acta* **1963**, *19*, 431−434.
(42) Woods, G. L.; Washington, J. A. Antibacterial susceptibility tests: dilution and disk diffusion methods, In: *Manual of Clinical Microbiology*; P. R., Murray, E. J., Baron, M.A., Pfaller, F. C., Tenover, R. H., Yolken Eds.; American Society of Microbiology: Washington, DC, USA, 1995.
(43) Wiegand, I.; Hilpert, K.; Hancock, R. E. Agar and broth dilution methods to determine the minimal inhibitory concentration (MIC) of antimicrobial substances. *Nat. Protoc.* **2008**, *3*, 163−175.
(44) Mosmann, T. Rapid colorimetric assay for cellular growth and survival: application to proliferation and cytotoxicity assays. *J. Immunol. Methods* **1983**, *65*, 55−63.
(45) Bruker, *APEX2*; Bruker AXS Inc.: Madison, Wisconsin, USA, 2012.
(46) Bruker, *SAINT*; Bruker AXS Inc.: Madison, Wisconsin, USA, 2012.
(47) Sheldrick, G. M. A short history of SHELX. *Acta Crystallogr., Sect. A: Found. Adv.* **2008**, *64*, 112−122.
(48) Bruker, *SADABS*. Bruker AXS Inc.: Madison, Wisconsin, USA, 2001.
(49) Sheldrick, G. M. Crystal structure refinement with SHELXL. *Acta Crystallogr., Sect. C: Struct. Chem.* **2015**, *71*, 3−8.
(50) Macrae, C. F.; Sovago, I.; Cottrell, S. J.; Galek, P. T. A.; McCabe, P.; Pidcock, E.; Platings, M.; Shields, G. P.; Stevens, J. S.; Towler, M.; Wood, P. A. Mercury 4.0: from visualization to analysis, design and prediction. *J. Appl. Crystallogr.* **2020**, *53*, 226−235.
(51) Spackman, P. R.; Turner, M. J.; McKinnon, J. J.; Wolff, S. K.; Grimwood, D. J.; Jayatilaka, D.; Spackman, M. A. CrystalExplorer: a program for Hirshfeld surface analysis, visualization and quantitative analysis of molecular crystals. *J. Appl. Crystallogr.* **2021**, *54*, 1006−1011.
(52) Spackman, M. A.; Jayatilaka, D. Hirshfeld surface analysis. *CrystEngComm* **2009**, *11*, 19−32.
(53) Wolff, S. K.; Grimwood, D. J.; McKinnon, J. J.; Turner, M. J.; Jayatilaka, D.; Spackman, M. A. *CrystalExplorer (Version 17.5)*; University of Western Australia: Perth, 2012.
(54) McKinnon, J. J.; Jayatilaka, D.; Spackman, M. A. Towards quantitative analysis of intermolecular interactions with Hirshfeld surfaces. *Chem. Commun.* **2007**, *37*, 3814−3816.
(55) Thomas, S. P.; Spackman, P. R.; Jayatilaka, D.; Spackman, M. A. Accurate lattice energies for molecular crystals from experimental crystal structures. *J. Chem. Theory Comput.* **2018**, *14*, 1614−1623.
(56) Lewars, E. G. Introduction to Quantum Mechanics in Computational Chemistry. In *Computational Chemistry: Introduction to the Theory and Applications of Molecular and Quantum Mechanics*; Springer International Publishing: Cham, 2016; pp 101−191.
(57) Lee, C.; Yang, W.; Parr, R. G. Development of the Colle-Salvetti correlation-energy formula into a functional of the electron density. *Phys. Rev. B: Condens. Matter* **1988**, *37*, 785−789.
(58) Francl, M. M.; Pietro, W. J.; Hehre, W. J.; Binkley, J. S.; Gordon, M. S.; DeFrees, D. J.; Pople, J. A. Self-consistent molecular orbital methods. XXIII. A polarization-type basis set for second-row elements. *J. Chem. Phys.* **1982**, *77*, 3654−3665.
(59) M.J., Frisch, G.W., Trucks, H.B., Schlegel, G.E., Scuseria, M.A., Robb, J.R., Cheeseman, G., Scalmani, V., Barone, G.A., Petersson, H., Nakatsuji, X., Li, M., Caricato, A., Marenich, J., Bloino, B.G., Janesko, R., Gomperts, B., Mennucci, H.P., Hratchian, J.V., Ortiz, A.F., Izmaylov, J.L., Sonnenberg, D., Williams-Young, F., Ding, F., Lipparini, F., Egidi, J., Goings, B., Peng, A., Petrone, T., Henderson, D., Ranasinghe, V.G., Zakrzewski, J., Gao, N., Rega, G., Zheng, W., Liang, M., Hada, M., Ehara, K., Toyota, R., Fukuda, J., Hasegawa, M., Ishida, T., Nakajima, Y., Honda, O., Kitao, H., Nakai, T., Vreven, K., Throssell, J.A., Montgomery, Jr., J.E., Peralta, F., Ogliaro, M., Bearpark, J.J., Heyd, E., Brothers, K.N., Kudin, V.N., Staroverov, T., Keith, R., Kobayashi, J., Normand, K., Raghavachari, A., Rendell, J.C., Burant, S.S., Iyengar, J., Tomasi, M., Cossi, J.M., Millam, M., Klene, C., Adamo, R., Cammi, J.W., Ochterski, R.L., Martin, K., Morokuma, O., Farkas, J.B., Foresman, D.J., Fox. *Gaussian 09, Revision D.01*, Gaussian, Inc.: Wallingford, CT, USA, 2009.
(60) Jamróz, M. H. Vibrational energy distribution analysis (VEDA): scopes and limitations. *Spectrochim. Acta, Part A* **2013**, *114*, 220−230.

https://doi.org/10.1021/acsomega.3c01469
ACS Omega 2023, 8, 13465−13477

(61) Johnson, R. D. *Precomputed vibrational scaling factors, in Computational Chemistry Comparison and Benchmark DataBase*; National Institute of Standards and Technology, 2019, https://cccbdb.nist.gov/vibscalejust.asp.
(62) Lu, T.; Chen, F. Multiwfn: a multifunctional wavefunction analyser. *J. Comput. Chem.* **2012**, *33*, 580−592.
(63) Emamian, S.; Lu, T.; Kruse, H.; Emamian, H. Exploring nature and predicting strength of hydrogen bonds: A correlation analysis between atoms-in-molecules descriptors, binding energies, and energy components of symmetry-adapted perturbation Theory. *J. Comput. Chem.* **2019**, *40*, 2868−2881.
(64) Labute, P. *Molecular Operating Environment (MOE)*; Chemical Computing Group Inc.: 1010 Sherbooke St. West, Suite #910, Montreal, QC, Canada, H3A 2R7, 2014.
(65) Labute, P. LowModeMD—implicit low-mode velocity filtering applied to conformational search of macrocycles and protein loops. *J. Chem. Inf. Model.* **2010**, *50*, 792−800.
(66) Marenich, A. V.; Cramer, C. J.; Truhlar, D. G. Universal solvation model based on solute electron density and on a continuum model of the solvent defined by the bulk dielectric constant and atomic surface tensions. *J. Phys. Chem. B* **2009**, *113*, 6378−6396.
(67) Yanai, T.; Tew, D. P.; Handy, N. C. A new hybrid exchange-correlation functional using the Coulomb-attenuating method (CAM-B3LYP). *Chem. Phys. Lett.* **2004**, *393*, 51−57.
(68) O'Boyle, N. M.; Tenderholt, A. L.; Langner, K. M. cclib: a library for package-independent computational chemistry algorithms. *J. Comput. Chem.* **2008**, *29*, 839−845.
(69) Dennington, R.; Keith, T. A.; Millam, J. M. *GaussView. 2016*, Semichem Inc.: Shawnee Mission, KS, *2016*.
(70) Humphrey, W.; Dalke, A.; Schulten, K. VMD: visual molecular dynamics. *J. Mol. Graph.* **1996**, *14*, 33−38 27−28,.
(71) *Discovery Studio Visualizer*; Accelrys Software Inc., 2009.

https://doi.org/10.1021/acsomega.3c01469
ACS Omega 2023, 8, 13465−13477